Journal of Materials Chemistry A

Accepted Manuscript

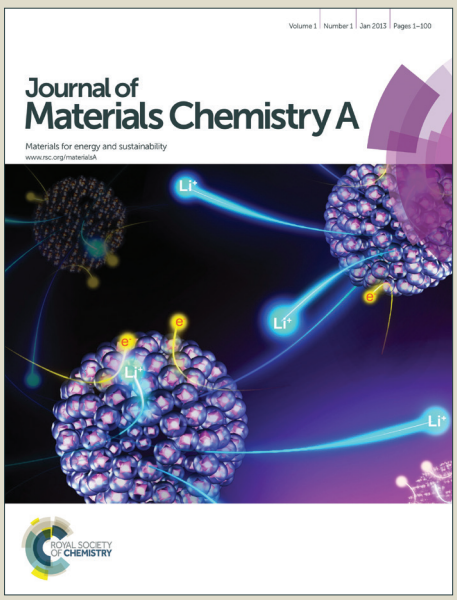

ROYAL SOCIETY OF CHEMISTRY

www.rsc.org/materialsA

Graphical abstract

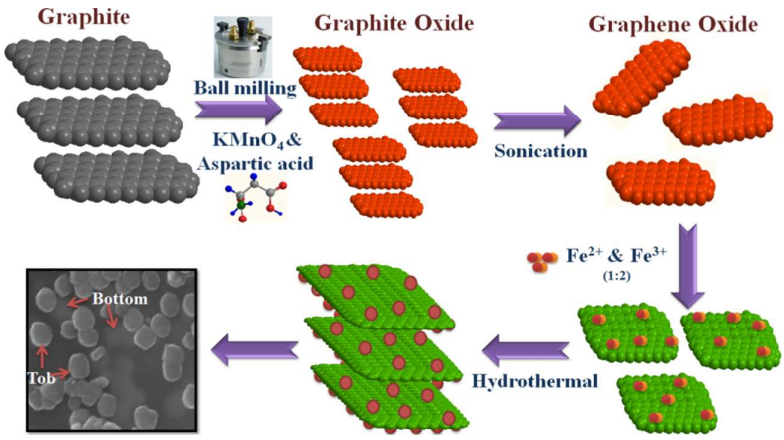

Journal Name

ARTICLE

Solvent Free Mechanochemical Synthesis of Graphene Oxide and Fe_3O_4/Reduced Graphene Oxide Nanocomposites for Sensitive Detection of Nitrite

Received 00th January 20xx,
Accepted 00th January 20xx

DOI: 10.1039/x0xx00000x

www.rsc.org/

G. Bharath,[a] Rajesh Madhu,[b] Shen-Ming Chen,[b] Vediyappan Veeramani[b], D. Mangalaraj and N.Ponpandian[a]*

Abstract

We report a versatile and eco-friendly approach to prepare the large scale defect free high quality graphene nanosheets from graphite by simple mechanochemical ball milling in the presence of $KMnO_4$ and aspartic acid. Two foremost concerns such as surface chemistry and physical properties must be considered for potential application of the functionalized ball milled graphene. The surface chemistry of the functionalized graphene has been studied through the anchoring of Fe_3O_4 nanoparticles with various particles loading (10, 20 and 30 %) can also be synthesized by simple hydrothermal process. The obtained samples were systematically studied by a variety of analytical and spectroscopic techniques to understand the structural, morphological, functional, compositional, electrical and magnetic properties. An electrochemical sensor was developed based on the prepared nanocomposite loaded on the glassy carbon electrode (GCE). The sensor based on the modified GCE exhibits good electrocatalytic activity, high sensitivity and stability for the detection of nitrite. The current response is linear over two different ranges between 0.5-58 µM and a wide range of 0.5 µM-9.5 mM with a low detection limit and sensitivity of 0.03 µM and 202.5 µA $mM^{-1}cm^{-2}$ respectively. In addition, the validation of applicability of the prepared biosensor was carried out by determining the nitrite in tap, river and rain water samples.

1. Introduction

Recently, research on graphene become one of the most exciting and rapidly growing areas in materials chemistry due to their potential real world applications. It has a unique 2D structure with sp^2- bonded carbon atoms with π electron cloud in a closely packed honeycomb structure. These single layers of graphene exhibit superior electronic properties obeying Dirac physics for promising electronic materials in upcoming carbon based electronic devices. The single and bilayer graphene sheets have zero band gap energy and therefore the charges are carried by massless particles.[1] However, the tri and few-layered graphene acts as a semi-metal and the band gaps are overlapped. The semi-metallic state is mainly due to the number of layers and defects states. Due to these outstanding properties of graphene, it has been considered in different potential applications such as nanoelectronics, field effect transistor, spintronics, tunnelling devices, dye-sensitized solar cells, super capacitors, batteries, nanophotonics, catalysis, gas sensor, electrochemical sensors, drug carrier and DNA biosensors.[2-5] All these qualities motivate the researchers to prepare graphene and their composites by simple methods with less structural defects for their potential applications. There are several methods have been developed for the preparation of graphene sheets including chemical exfoliation, chemical vapour deposition, epitaxial growth on SiC, scotch tape, unzipping of carbon nanotubes, mechanochemical cleavage and other organic synthetic protocols.[5-11] Though, the large scale production of graphene with high quality is still a challenging task for the researchers. However, the mechanochemical method is one of the best methods to synthesize few layers of graphene sheets with less structural defects.[12-13] The high speed of the planetary rotation and the collision of stainless steel vials and balls generate sufficient kinetic energy for bond cleavages in C-C aromatic graphite structure in the presence of organic and inorganic reactive species. It also introduces the functional groups on the creaked edges, surfaces and basal planes of the graphene during the milling process.

[a] Department of Nanoscience and Technology, Bharathiar University, Coimbatore 641 046, India. *Corresponding authors e-mail: ponpandian@buc.edu.in, Phone: + 91-422-2428423.
[b] Department of Chemical Engineering and Biotechnology, National Taipei University of Technology, Taipei 10608, Taiwan.

In contrast, it is necessity to consider the surface chemistry and physical properties for the potential multifunctional applications of functionalized graphene. Several recent reports explain the synergistic coupling between inorganic nanoparticles and functionalized graphene sheet improves the performance of nanomaterials. The graphene based nanocomposites with numerous nanoparticles such as metal, metal oxides, metal hydroxides, conducting polymer, ceramics and sulphide have hold potential to enlarge the prospects of their usage. However, the reduced graphene oxide (RGO)-Fe_3O_4 nanocomposite provides excellent magnetic, electrical, catalytic and mechanical properties. It also has been used in various applications such as electrochemical sensors, heavy weight metals adsorption, biomedical application, environmental remediation, spintronics *etc*.[13-22] It also exhibits an excellent electrochemical activity for the determination of various organic and inorganic compounds in different water sources. Numerous reports were already available for the selective and sensitive detection of inorganic pollutants such as hydrazine, nitrite, nitrate and mercury by using electrochemical techniques.

Nitrite is an inorganic pollutant to the environment and human health which was widely there in food, fertilizers and corrosion inhibitor. The excessive nitrite in human body can lead to interact with amines to form carcinogenic nitrosamines, resulting in serious hazards to human and animal health. Nitrite is always present in water distribution system such as sea, ground, lake, river and rain water due to its usage in fertilizers. Therefore, the accurate determination of nitrite is very important in environmental and biological safety. Presently, many techniques were available for the determination of nitrite such as spectrophotometry, chemiluminescence, molecular absorption spectroscopy, fluorescence, chromatography and electrochemistry. Among these, the electrochemical analytical method has been widely used for the determination of nitrite due to its excellent reliability, simple operation, sensitivity, selectivity, quick response and cost effectiveness. However, the direct determination of nitrite at bare glassy carbon electrode (GCE) normally suffers because of their large potential. Therefore, the electrodes will be modified with different electro catalysts to decrease the operating potential. The electrodes modified with graphene and graphene based metal oxide nanocomposites exhibit an excellent electrochemical responses towards the detection of nitrite.[18-31]

Herein, we report an economically viable and environmental friendly high energy ball mill was used to synthesize graphene oxide from natural graphite flakes with the presence of $KMnO_4$ and aspartic acid. In addition, the Fe_3O_4 nanoparticles were uniformly dispersed on both sides of the prepared 2D RGO sheets by using a one pot facile hydrothermal process. The size, shape and particle-particle interaction of Fe_3O_4 nanoparticle strongly depends on the concentration of iron precursor. The effect of nanoparticle loading (10, 20 and 30 weight % Fe_3O_4) on RGO sheets with their structural, morphological, electrical and magnetic properties were investigated by using different analytical techniques. The glassy carbon electrode modified with this novel Fe_3O_4/RGO nanocomposite exhibits admirable electrocatalytic activity to develop sensitive sensor for the electrochemical detection of nitrite. The fabricated electrochemical sensor exhibits significant sensitivity, selectivity and desired detection limits and also this was further extended for real time sample analysis.

2. Experimental

2.1 Materials

All the chemicals were of analytical grade and used as received without further purification. Graphite flakes (~105 µm flakes), potassium permanganate ($KMnO_4$), aspartic acid, ferrous chloride tetrahydrate ($FeCl_2{\cdot}4H_2O$) and ferric chloride hexahydrate ($FeCl_3{\cdot}6H_2O$) were supplied by Sigma Aldrich. Sodium hydroxide (NaOH), acetone, hydrochloric acid 5% (HCl) and ethanol were purchased from Himedia Laboratory Pvt. Ltd.

2.2. Solvents free mechanochemical synthesis of graphene oxide via high energy ball mill

In a typical procedure, the natural graphite was milled in a planetary ball-mill (Pulverisette 7, Fritsch) in the presence of $KMnO_4$ and aspartic acid at 400 rpm for 24 h with stainless steel vial and ball with the ball to powder weight ratio of 10:1. The final product was washed with 5% HCl solution to remove the residues of the oxidants and metal impurities. This was further washed with deionized water several times until the pH become neutral and dried under vacuum oven at 70^{o}C for 24 h.

2.3. Synthesis of Fe_3O_4/RGO nanocomposite by hydrothermal process

In a typical process, 30 mg of graphene oxide was suspended in 30 mL of deionized water by ultrasonic dispersion for 5 h to form a stable brown color graphene solution and the supernatant was collected for further experimental process. Subsequently, 50 mM of $FeCl_2{\cdot}4H_2O$ were dissolved in the above solution and pH value was adjusted between 10-11 by adding 30 % of ammonium hydroxide solution (NH_4OH). This solution was transferred to the Teflon-lined stainless steel autoclave and it was placed in an oven at 180 ^{o}C for 12 h and it was cooled down naturally to room temperature. The final block color precipitate was washed with double distilled water and ethanol several times. Finally, the sample was dried in vacuum oven at 70^{o}C for overnight before further characterization. Another experiments were conducted with different particles (Fe_3O_4) loadings (10, 20 and 30%) on RGO by same property conditions.

2.4. Characterization

The X-ray diffraction (XRD) pattern were recorded at room temperature using a PANalytical X'Pert-Pro diffractometer with Cu $K\alpha_1$ radiation (λ= 1.5406 Å). The morphology and elemental analysis of the composite was determined by high resolution transmission electron microscopy (HRTEM, JEOL, JEM-3000F) and field emission scanning electron microscopy (FEI Quanta – 250) with EDX. The infrared spectra of the samples were obtained by using a Fourier transform infrared (FTIR) spectrometer (Bruker Tensor 27, Germany). Raman spectra was recorded using a JY-1058 Raman spectrometer using 520 nm laser source. UV-Visible spectral analysis was done by using JoscoV-650 spectrophotometer. The X-ray photoelectron spectroscopic (XPS) measurements were done by Kratos Axis Ultra-DLD X-ray photoelectron spectrometer (Manchester, U.K). Surface area and pore size distribution of a nanocomposite was determined using a micromeritics ASAP 2020 surface area analyzer.

2.5. Fabrication of the Fe_3O_4/RGO modified electrode

The as-prepared Fe_3O_4/RGO was dispersed in ethanol and sonicated for 2 h to obtain a stable dispersion. Prior to modification, the GCE surface was carefully polished with mirror finish with alumina slurry. Then, it was washed with distilled water and ultrasonicated in ethanol-containing water for a few minutes. Approximately 6 ml of Fe_3O_4/RGO dispersion (optimized concentration) was drop-cast on the pre-cleaned GCE and dried in hot air oven at 30° C. Then, the Fe_3O_4/RGO modified GCE was gently rinsed few times with double distilled water to remove the loosely bound nanoparticles. The fabricated Fe_3O_4/RGO modified electrode was used for further electrochemical experiments and all the experiments were performed at room temperature in an inert atmosphere.

3. Results and Discussion

3.1 Surface chemistry and physico-chemical properties of ball milled graphene and Fe_3O_4/RGO nanocomposites

The mechanochemical reaction driven by ball milling introduces various functional groups such as epoxy, hydroxyl (-OH) and carboxylic (-COOH) on the basal plan as well as the broken edges of graphite in the presence of reactive inorganic and organic species in a solid condition. The significance of this process is cost effective, high yield, mass production, introduction of various functional groups on the surfaces and edges of graphene.

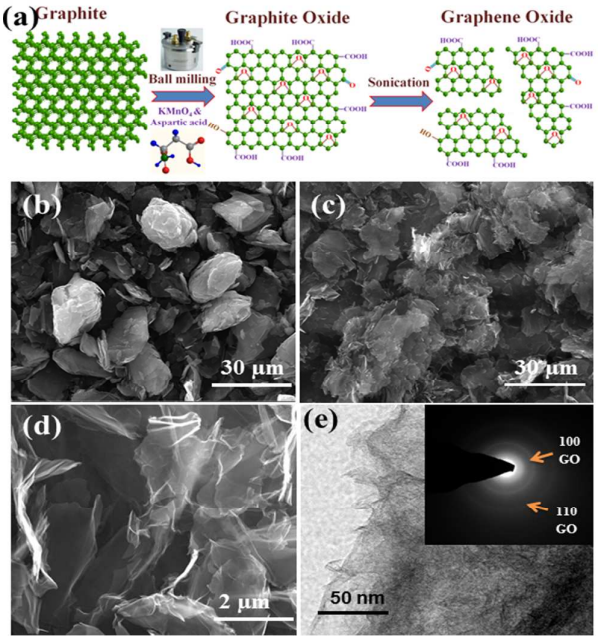

Fig. 1 (a) Schematic illustration of synthesis strategies of GO by planetary ball milling in the presence of $KMnO_4$ and aspartic acid, (b) FESEM image of as-received natural graphite flakes, (c) FESEM image of ball milled graphite flakes, (d) and (e) FESEM and TEM with SAED pattern images of exfoliated graphene oxide.

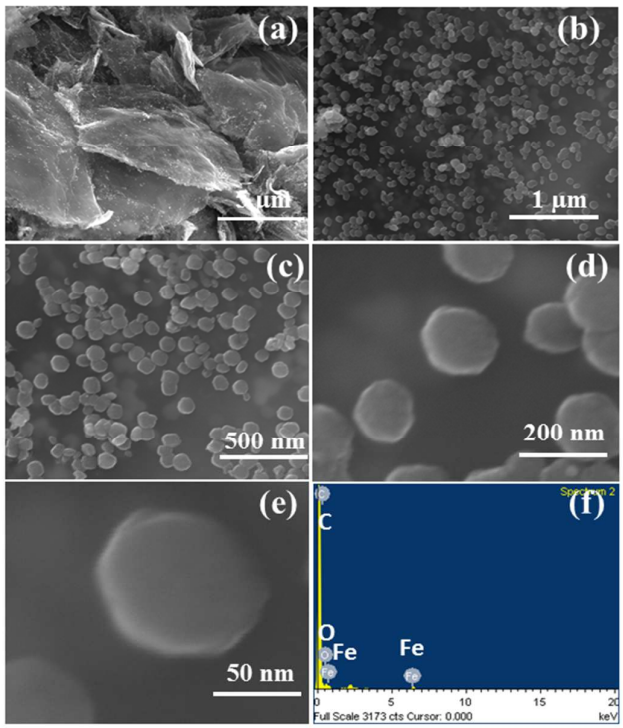

Fig. 2 (a-e) FESEM images of Fe_3O_4/RGO nanocomposite with different magnifications and (f) EDX spectrum of Fe_3O_4/RGO nanocomposite.

Schematic illustration in Fig. 1(a) shows the epoxy and carboxylic group functionalization on the surfaces and broken edges of graphite synthesized by ball milling the bulk graphite. The high energy ball produces sufficient kinetic energy for making cleavage in the graphitic C-C bonds in the presence of $KMnO_4$ aspartic acid. This kinetic energy compensates the weak forces of Van der Waals attraction between two adjacent π-π stacked graphite layers for bond cleavages for the C-C aromatic graphite structure.

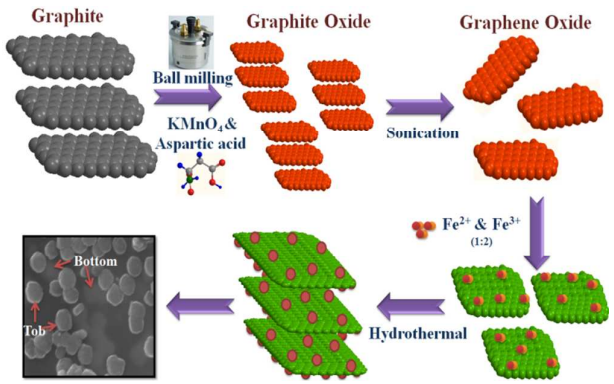

Fig. 3 Schamatic representation of the new strategy for the formation mechanism of Fe_3O_4/RGO nanocomposite synthesized by hydrothermal process at 180°C for 12 h.

Also, the reactive species of $KMnO_4$ intercalated between two adjacent carbon layers and aspartic acid could effectively involve in the functionalization at the edges of graphite resulting is a very few layer of graphene obtained within the rapid milling time. This milled product was suspended in water and sonicated for 3 h to obtain stable brown color solution. Normally, the oxygen containing groups such as epoxy (C-O), hydroxyl (-OH) and carboxylic ($-COO^-$) decorate the basal planes on the interior of multi-layered stacks of graphite and periphery of the planes. Thereby, the Van der Waals force is weak between the adjacent layers and this enables the milled graphite oxide are highly dispersible in water. Further, we obtained the negative zeta potential of -40 mV for the ball milled sample measured by the zeta potential analyser.

These results demonstrate that the strong repulsive force arises between the negatively charged oxygen containing functional groups on the surfaces of graphene generated from the chemical reaction with reactive species during the ball milling process. FESEM micrographs in Fig.1 (b&c) show an obvious size reduction from larger grain size of 60-80 µm for natural graphite flakes to smaller grain size of 2-5 µm for graphite oxide by planetary ball milling. Figure 1 (d & e) shows the FESEM and TEM images of exfoliated graphene sheets homogeneous dispersion, it contains few layer of carbon and is highly transparent under beam of electron.

Inset Fig.1(e) shows the corresponding SAED pattern of GO, which was exhibits that 110 and 100 are associated to hexagonal lattice structure of the carbon atoms. The surface chemistry and physical properties are two important factors for potential multifunctional applications of the graphene and their nanocomposites. The surface chemistry of the functionalized ball milled graphene has been studied through the anchoring of Fe_3O_4 nanoparticles with different loading of 10, 20 and 30 % Fe_3O_4. Figure 2 (a-e) shows the FESEM images with different magnifications. It depict that the Fe_3O_4 nanoparticles were grown on the surface, basal plane and edges of graphene sheets with uniform dispersion and narrow size distribution.

The particle sizes are in the range of 70-90 nm (average: 85 nm). Figure 2 (a & b) shows the agglomeration free individual graphene sheets with uniformly distributed Fe_3O_4 nanoparticles on the surfaces, basal and edges of the RGO sheets. Further, the high resolution FESEM image evidences that Fe_3O_4 nanoparticles are uniformly dispersed on both sides of the RGO as shown in Fig 2 (c&d). The morphology of the individual Fe_3O_4 nanoparticles is clearly observed by using high resolution FESEM image as shown in Fig 2(e). The EDX spectrum in Fig 2(f) shows the elements carbon (C), oxygen (O) and iron (Fe) are presented and no other impurity was detected.

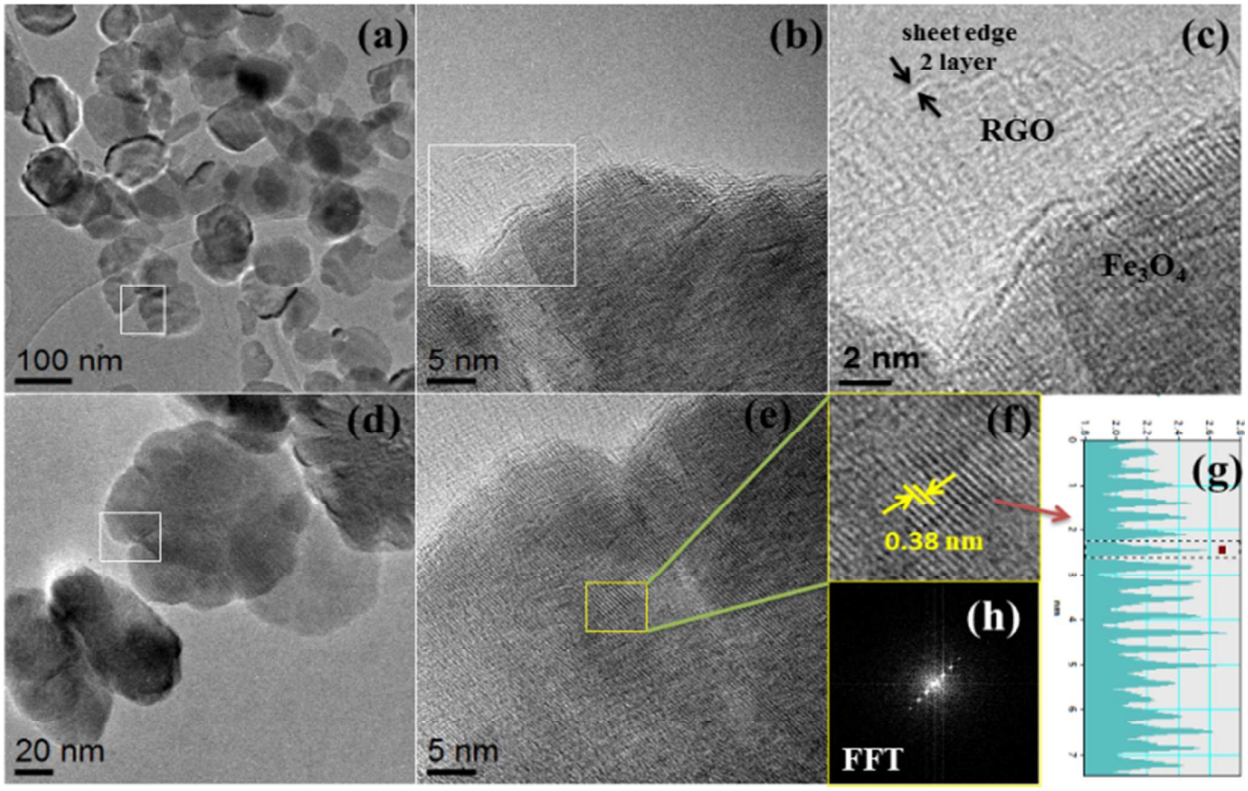

Fig.4 HRTEM images of the Fe_3O_4/RGO nanocomposites with stepwise increased magnifications (a-f), (g) corresponding intensity profile and (h) Fast Fourier transform (FFT) pattern of lattice fringes for nanostructured Fe_3O_4.

Mostly, the oxygenated functional groups provide not only water dispersibility and also lead to the formation of nanoparticles on surfaces, basal plane and edges of the graphene. Schematic representation of the synthesis strategies and possible nucleation growth of the Fe_3O_4/RGO nanocomposites are shown in Fig. 3. The widely accepted mechanism for the synthesis of Fe_3O_4 nanoparticles dispersed on graphene is the electrostatic attraction between the positively charged metal ions and polarized bonds of the negatively charged functional groups of the graphene oxide sheets. Briefly, the as-milled graphite oxide was dispersed in water and sonicated for 4 h to obtain stable brown color solution. The supernatant was collected for further experimental procedure and the required molar concentration of the Fe^{2+} ions was added to graphene oxide solution. The Fe^{2+} ion in the solution was selectively bonded with oxygenated groups such as epoxy, hydroxyl and carboxyl group of graphene oxide through the electrostatic interactions and this nucleation process is called redox hybridization process. The graphene oxide act as an oxidizing agent it efficiently increases the oxidation state of the iron ions from Fe^{2+} to Fe^{3+}, as it's described in eqn. 1. In an alkaline medium the initial nucleation of Fe_3O_4 were started on the surfaces, basal plane and edges of the two dimensional RGO sheets. During the hydrothermal reaction process, the polar oxygenated functional groups on the graphene oxide sheets serves as the anchoring sites for Fe_3O_4 nanoparticles and it was grown on both sides of 2D RGO sheets. The detailed redox reaction mechanism is described in eqn (2) and (3)

$$2\,Fe^{2+} + GO \rightarrow 2\,Fe^{3+} + RGO \quad (1)$$

$$2\,Fe^{3+} + Fe^{2+} + 8OH^{-} \rightarrow Fe_3O_4 + 4H_2O \quad (2)$$

$$3\,Fe^{2+} + GO\,(8OH^{-}) \rightarrow Fe_3O_4 + 4H_2O + RGO \quad (3)$$

The Fe_3O_4 nanoparticles grown on both top and bottom of the RGO sheets may be due to the epoxy (C-O) and hydroxyl (-OH) ions present in both sides of RGO sheets. Also the Fe_3O_4 nanoparticles were present in the edges of RGO and this may be due to the –COOH ions present in the edges of RGO sheets.

The HRTEM images and fast Fourier transform (FFT) pattern were recorded to characterize the fine structures in the morphology and crystalline structure of Fe_3O_4/RGO nanocomposites. Figure 4 (a-f) shows the HRTEM images of the Fe_3O_4/RGO nanocomposites with different magnifications. The HETEM images in Fig.4 (a-c) shows the well dispersed Fe_3O_4 nanoparticles in the surfaces of RGO sheets with average particle size of 90 nm. Also, a small foldings were observed in the edges of RGO and it contains only 2 layers of graphene. The HRTEM image in Fig.4 (f) shows the characteristic lattice fringes of Fe_3O_4 nanoparticles in the surrounding of RGO matrix. The lattice fringes with the d-spacing of 0.38 nm corresponds to the 111 plane of $Fe3O_4$. Figure.4 (g) shows the HRTEM intensity contrast profile recorded along the marked line in Fig.4 (f) shows the lattice distance of 0.38 nm. These values are in good agreement with the standard data of Fe_3O_4 (JCPDS no. 65-3107). The continuous and clear lattice fringes in Fig.4(f) combined with the Fast Fourier transform (FFT) pattern shown in Fig.4(h) reveals the single-crystalline nature of Fe_3O_4 nanoparticles.

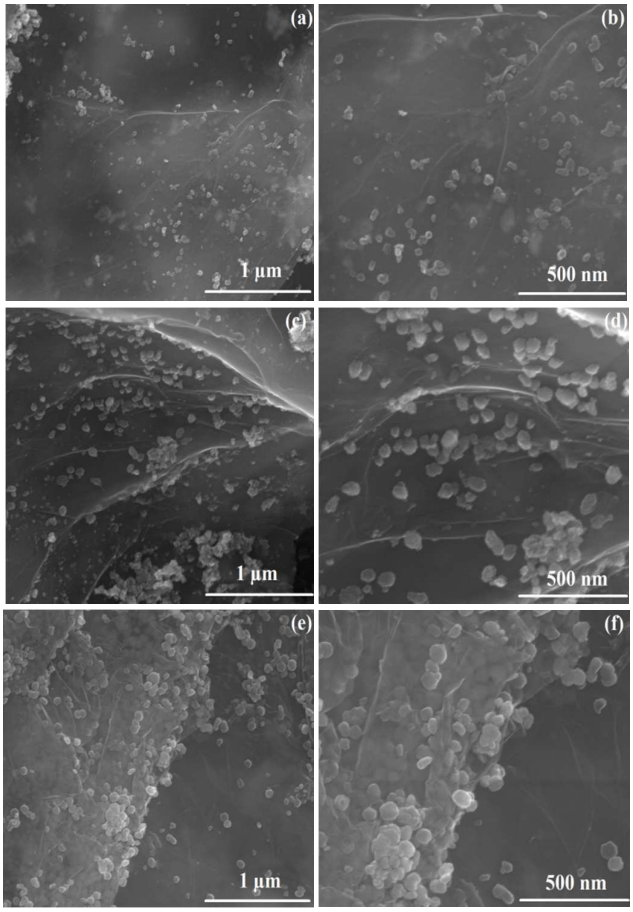

Fig. 5 FESEM images of Fe_3O_4/RGO nanocomposites with different percentage of Fe_3O_4 loading with different magnifications. (a, b) 10%, (c, d) 20% and (e, f) 30%.

Figure 5 (a-f) shows the Fe_3O_4/RGO nanocomposites with different loading of 10, 20 and 30% of Fe_3O_4. Obviously, the spherical shape Fe_3O_4 nanoparticles were directly grown on both sides of RGO sheets. Figure 5 (a&b) shows the FESEM images with higher magnification for 10% of Fe_3O_4 loading on RGO sheets, clearly shows the size of 20 nm with spherical like morphology. The increased loading of Fe_3O_4 to 20 % correspondingly increases the particles density on the surfaces of RGO sheets and also increases the size of the nanoparticles to 37 nm as shown in Fig 5(c&d). The higher density of Fe_3O_4 with the diameter 85 nm were grown on RGO sheets by increasing the Fe_3O_4 loading to 30%, as shown in Fig 5 (e& f). This result confirms, increasing the loading % of Fe_3O_4 increases the density and diameter. During the nucleation growth process, increasing Fe^{2+} concentration in the reaction, increases the solubility and more number of nuclei is dissolved for growth resulting in larger aggregation of nanoparticles. Thus, the minimum size of the nanoparticles increases with increased concentration of the Fe^{2+} ions, this may be reason for the larger size distribution of particles grown on RGO sheets.

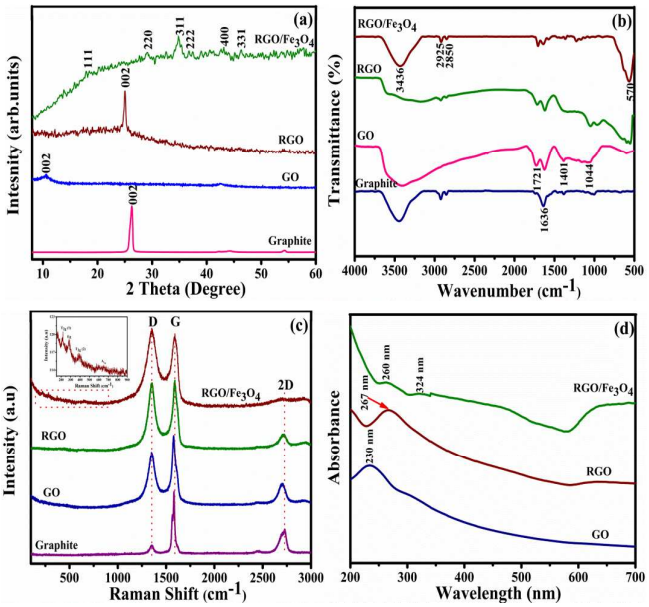

Fig. 6 (a) X-ray powder diffraction patterns, (b) FTIR spectra, (c) Raman spectra and (d) UV-vis spectra of Graphite, GO, RGO and Fe_3O_4/RGO nanocomposite.

X-ray diffraction pattern of solid natural graphite flakes, graphene oxide, reduced graphene oxide and Fe_3O_4/RGO nanocomposites are shown in Fig 6 (a). The natural graphite flakes exhibit a strong diffraction peak at 26.5° (002) with corresponding interlayer d-spacing of 0.34 nm with expected 3 dimensional diffraction lines from hexagonal graphite (h-graphite). A large peak shift from 26.5° to 11.5° was observed for the ball milled graphite in the presence of $KMnO_4$ and aspartic acid with relatively increased interlayer d-spacing of 0.87 nm. The increased interlayer d-spacing may be due to the oxygen containing functional groups are attached on edges and both sides of the graphite sheets. The reduced graphene oxide (RGO) sheets obtained by a simple hydrothermal treatment of graphene oxide (GO) at 180 °C for 12 h.[23] After hydrothermal reduction process, a sharp diffraction peak occurs at 24.3° with the interlayer d-spacing of 0.45 nm for RGO due to the reduction of graphene oxide and the restoration of C-C (sp^2) bonding. However, the d-spacing of RGO is higher than that of well-ordered pure natural graphite, signifying the presence of some residual oxygenated groups in RGO. The XRD pattern for the Fe_3O_4/RGO nanocomposites exhibits *face centered cubic* structure (JCPDS No. 65-3107) with an average grain size of 60 nm , calculated from Scherer formula. Further, no characteristic peaks were observed for impurities. The observation in the XRD patterns confirms the Fe_3O_4 nanoparticles are successfully grown on both sides of RGO by simple hydrothermal process.

The surface chemistry of bonding nature and chemical structure for the natural graphite flakes, graphene oxide, RGO and Fe_3O_4/RGO nanocomposites were further studied by FTIR spectroscopy and the corresponding spectra are shown in Fig 6 (b). The FTIR spectrum for the pure graphite shows a sharp intense peaks at 1636 and 3436 cm^{-1}, which corresponds to stretching vibration of C=C and bending modes of water associated with KBr used for the preparation of the FTIR pellets. After ball milling of graphite in the presence of $KMnO_4$ and aspartic acid, the surface and edges of graphite were functionalized with oxygenated groups. The intense peaks at 1240 and 1721 cm^{-1} corresponds to stretching vibration of epoxy (C-O) and stretching of carboxylic (C=O) groups. Although the oxygenated functional groups were intensely located at surfaces and edges of the graphene oxide sheets, it was further reduced by post reduction of hydrothermal process resulting in partially reduced epoxy, hydroxyl and carboxylic groups as shown in FTIR spectrum of RGO. The FTIR spectrum for the Fe_3O_4/RGO nanocomposite exhibits intense peaks at 570 and 600 cm^{-1} associated with the lattice adsorption of iron oxide (Fe-O).

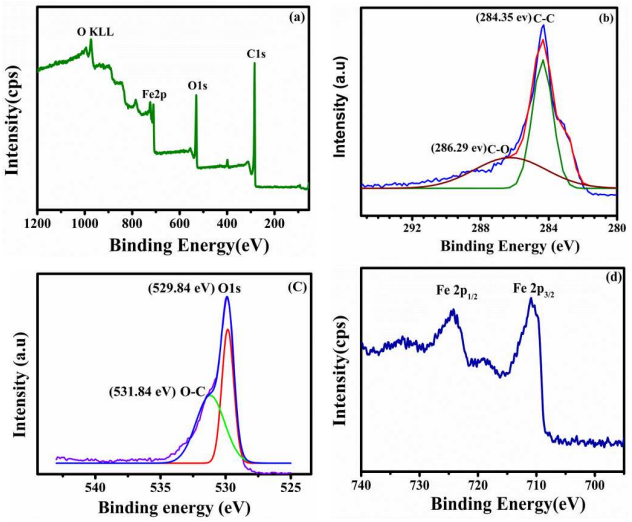

Fig. 7 (a) The XPS wide scan spectrum of Fe_3O_4/RGO nanocomposite, (b) high resolution spectrum of C1s, (c) O1s and (d) Fe2p.

Raman spectroscopy is widely utilized as a powerful analytical technique to characterize carbon based nanomaterials. The characterization of the Raman spectra of graphene prompted enormous effort to understand quantifying defects, phonon, phonon-electron, electron-electron interaction and identifying number and orientation of graphene layers. Figure 6 (c) demonstrates Raman spectrum of pure graphite, graphene oxide, RGO and Fe_3O_4/RGO nanocomposite and the spectra consist of three prominent peaks, namely the D band, G band and 2D band. The intense bands attributed at 1331, 1578 and 2694 cm^{-1} corresponds to D, G and 2D, respectively. The D band is the edge-induced disordered related to the presence of sp^3 defects and the G band is associated to the in-plane vibration of sp^2(C=C) aromatic carbon structure which is a particularly degenerate phonon mode of E_{2g} symmetry at the Brillouin zone centre. The intense band observed at 2694 cm^{-1} is associated to 2D band due to the second-order two phonons with opposite momentum in the highest optical branch adjacent to the K point of the Brillouin zone. An order and disorder structure of the graphene has been intensely observed by the intensity ratio (I_D/I_G) between D and G band. A universal observation is that the higher disorder graphene leads to a broad D band with higher relative intensity then the G band.

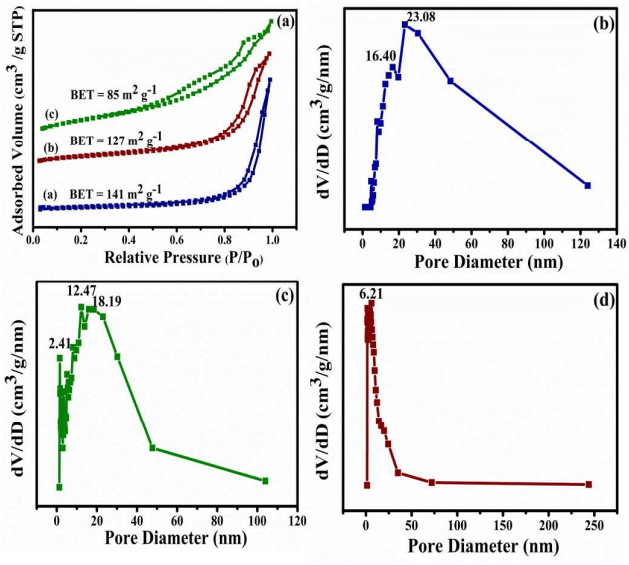

Fig. 8 (a) Nitrogen-adsorption/desorption isotherms of different loading of Fe_3O_4/RGO nanocomposites. Pore size distribution of (b) 20, (c) 40 and (d) 60 %

The intensity ratio (I_D/I_G) of 0.15, 0.41, 0.71 and 1.1 corresponds to pure graphite, graphene oxide, RGO and Fe_3O_4/RGO nanocomposite, respectively. Based on the above results the intensity ratio of the graphene oxide shows an enhanced value compared to pure graphite, representing the presence of localized sp^3 defects in the sp^2 (C=C) network upon oxidation of the graphite. After reduction, the D and G band was shifted and increases the intensity ratio of RGO due to decrease in the average size of sp^2 domains upon the hydrothermal reduction process. The 2D band has been extensively used to determine the number of layer of graphene.

The sharp broadened shaped 2D bands of graphene oxide and RGO exhibits few layer of carbon and conceivable that our samples are less disordered sp^2 aromatic structure. Therefore, the large scale synthesis of ball milled graphene exhibits that graphene contain few layers with less disordered sp^2 aromatic carbon structure, which agreed with the graphene synthesized from modified hummer's methods. The left inset enlarged Raman spectra of Fe_3O_4/RGO provide the complete structural investigations of magnetite phases from the nanocomposite. The intense band attributed at 669 cm^{-1} can be ascribed to magnetite A_{1g} active mode and less intense peaks at 400, 309 and 220 cm^{-1} correspond to the Raman active modes of T_{2g} (1), Eg and T_{2g} (2), for magnetite.

Further the chemical structure, reduction process and structural changes of graphene oxide have been observed through UV-vis absorption spectroscopy. Figure 6(d) shows the UV absorption spectra for graphene oxide, RGO and Fe_3O_4/RGO nanocomposites. The UV spectra of graphene oxide exhibits two absorption peaks at 230 and 303 nm corresponds to π-π* transitions of aromatic C-C bonds and n-π* transition of C=O bonds, respectively.

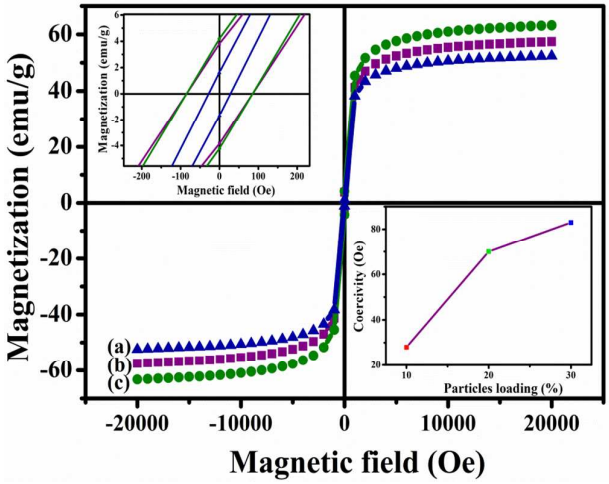

Fig. 9 Room temperature hysteresis loop for the Fe_3O_4/RGO nanocomposites (a) 10, (b) 20 and (c) 30% of Fe_3O_4 loading at room temperature. Top and bottom inset shows the coercivity variation of the samples.

The absorption peaks of RGO and Fe_3O_4/RGO nanocomposites corresponding to the π-π* transitions of aromatic C-C bonds red shifted to 267 nm after the hydrothermal treatment cause to restoration of the electronic conjugation of C=C bands in the graphene sheets. XPS was effectively employed to analyse the structural composition of Fe_3O_4/RGO nanocomposite. The XPS spectrum in Fig 7 (a) shows the wide spectrum of Fe_3O_4/RGO nanocomposite which exhibits three intense peaks at 286, 530 and 711 eV corresponds to carbon (C1s), oxygen (O1s) and Fe2p respectively. Figure 7 (b) shows the high resolution XPS spectrum for C 1s contain non-oxygenated aromatic sp^2 carbon ring (C-C) at 284.5 eV and oxygenated functional group of carbon sp^2 C-O attributed at 286.29 eV. The high resolution XPS spectrum of O1s in Fig 7 (c) shows two intense peaks at 529.84 and 531.84 eV for the anionic oxygen in magnetite and residual oxygen functional groups present in RGO sheets.

Figure 7(c) shows the high resolution XPS spectrum of Fe2p, which exhibits two prominent peaks attributed at 711.3 and 724.5 eV, corresponding to the $Fe2p_{3/2}$ and $Fe2p_{1/2}$ spin-orbit intense peaks of pure magnetite (Fe_3O_4). Thus the result indicates the formation of Fe_3O_4 nanoparticles on the surfaces of the RGO sheets. The specific surface area (SSA) and pore size distribution of the RGO loaded with different weight percentage of 10, 20 and 30% of Fe_3O_4 nanocomposite were further studied by adsorption-desorption experiment. Figure 8 (a-d) shows the BET surface area and corresponding BJH pore size distribution of the different nanocomposites. The isotherms of 10, 20 and 30 % loaded Fe_3O_4 nanocomposite exhibits a type IV isotherm corresponding to the mesoporous materials with a relative pressure between 0 to 1. It exhibits a specific surface area of 141, 127 and 85 m^2g^{-1} with an average pore size distribution of 18, 11 and 6.2 nm for the 10, 20 and 30% Fe_3O_4 loaded on RGO nanocomposites respectively. This clearly indicates that the increase in Fe_3O_4 loading on graphene significantly decreases the specific surface area and pore size of the nanocomposites. This may be due to more number of Fe_3O_4 nanoparticles occupies the surfaces of RGO and thereby it reduces the specific surface area.

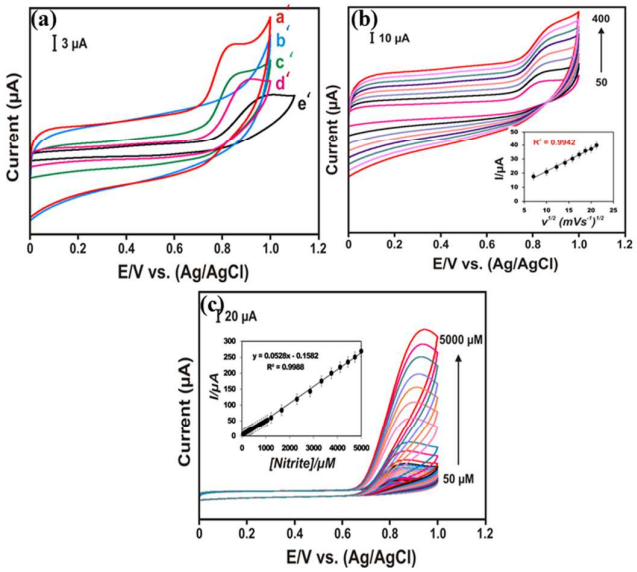

Fig. 10 (a). Cyclic voltammograms (CVs) of the (a') 30 , (b') 20, (c') 10 % of Fe_3O_4 loaded on Fe_3O_4/RGO nanocomposites modified GCE, (d') pure RGO and (e') bare GCE in 0.1 M PBS at pH 4 containing 50 μM nitrite. Scan rate: 50 Mv s^{-1}; (b) CVs for 30% Fe_3O_4 loaded on Fe_3O_4/RGO nanocomposites modified GCE with different scan rates (50-400 mVs^{-1}) in 0.1 M PBS at pH 4 containing 50 μM nitrite Inset: peak current (Ip) vs. (scan rate)$^{1/2}$ $(mVs^{-1})^{1/2}$ and (c) CV curves of 30 % of Fe_3O_4/RGO modified GCE under various nitrite concentrations of 50-5000 μM. Inset; cathodic reduction peak current (I_{pc}) *vs* nitrite concentration.

The magnetic properties of the Fe_3O_4 loaded on RGO has been intensely evaluated at room temperature using a vibrating sample magnetometer (VSM) by measuring the hysteresis with an applied magnetic field of -2 to 2 KOe. Figure 9 (a-c) shows the magnetic hysteresis loops for 10, 20 and 30 % loading of Fe_3O_4 nanoparticles on RGO sheets. The saturation magnetization (M_s) obtained from the hysteresis loops are 51, 58 and 68 emu/g for 10, 20 and 30 % Fe_3O_4 respectively. The inset in Fig.9 shows the coercivity (H_c) of the samples, which are 27, 72 and 81 Oe. All these magnetic parameters are associated with the FESEM images and surface area of the nanocomposites. Generally, the increase in particle size increases the saturation magnetization and coercivity. However, increasing Fe concentration during the nucleation process causes larger solubility and more number of nuclei is dissolved for growth resulting in larger aggregation of nanoparticles. The saturation magnetization and coercivity of the nanocomposites mostly changes by two parameters. The increase in coercivity with increasing particle size most possibly due to shape anisotropy correlated with the faceted growth of the Fe_3O_4 particles and the saturation magnetization from Fe ions on the octahedral sites.

3.2 Electrochemical properties

The electrocatalytic capability of Fe_3O_4/RGO nanocomposites was evaluated by cyclic voltammogram (CV), differential pulse voltammetry (DPV) and amperometric current-time (*i-t*) curve techniques using nitrate as analyte.

3.2.1 Cyclic Voltammogram (CV)

The electrocatalytic activity of the Fe_3O_4/RGO nanocomposites with 50 μM of nitrite in 0.1 M PBS (pH 4) was evaluated by cyclic voltammogram (CV). Figure 10 (a) shows the CV responses of different electrodes such as bare GCE, pure RGO, 10, 20 and 30 % Fe_3O_4 loaded RGO nanosheets. There was no signal observed at the surface of GCE without nitrite. The addition of 50 μM of nitrite in bare GCE exhibits not much difference in the CV curve with a weak peak current at E_{pa} (1 V). Interestingly, an obvious signal has been observed at 0.8 V for 30% Fe_3O_4 loaded RGO nanocomposites modified GCE, which is a very lower oxidation potential than the bare GCE, pure RGO, 10 and 20% of Fe_3O_4 loaded RGO. The cyclic voltammogram shows the oxidation peak potential of NO_2^- on the surface of Fe_3O_4/RGO nanocomposite modified electrode shifted negatively to 0.8 V than that of 1 V of bare GCE. Among them, 30% of Fe_3O_4 loading on RGO nanocomposite shows a large anodic peak current with favorable negative potential shift that causes the oxidation of nitrite and corresponding oxidation mechanism of NO_2^- to NO_3^- is as follows,

$$NO_2^- + H_2O \rightarrow NO_3^- + 2H^+ + 2e^- \quad (4)$$

The enhancement in peak current indicates the Fe_3O_4/RGO nanocomposite modified electrode could efficiently provide large surface area and higher concentration of Fe_3O_4 nanoparticles promotes the electro catalytic oxidation of NO_2^-. Moreover, the Fe_3O_4/RGO nanocomposite provides large adsorption sites for the adsorption of negatively charged ions of nitrite due to their high specific surface area (SSA). Therefore, the higher SSA leads to accumulate more nitrite ions on the proposed surface of electrodes resulting in increase of electron transfer capacity.

Figure 10 (b) shows the influence of scan rate on electrochemical activity of 30 % Fe_3O_4 loaded on RGO nanocomposites modified GCE, also studied by measuring the CV with different scan rates of 50-400 mVs^{-1} in 0.1 M PBS (pH 4) containing 50 μM nitrite. The CV curves clearly shows that the oxidation peak current (I_{pa}) increases gradually with increasing scan rates, although the peak potential (E_{pa}) was shifted positively. Therefore the I_{pa} increases linearly with scan rates, representing a diffusion controlled electrocatalytic process. The inset Fig 10 (b) shows that the I_{pa} value shows a linear dependence with square root of the scan rates which may be expressed by a linear regression equation as $E_{pa}(V)= 2.51 + 7.818\ V^{1/2}$ with correlation coefficient of R^2=0.9942. All these results obviously confirms and the eqn (4) can be expressed that the overall nitrite oxidation reaction process is a second-order homogeneous disproportionation process and the NO_3^- is the only plausible final product. Figure 10 (c) shows CV responses observed for various concentrations of nitrite at 30 % of Fe_3O_4/RGO nanocomposites modified GCE in 0.1 M PBS at pH 4. The nitrite concentration was increased by adding several nitrite concentrations of 50-5000 μM into the solution. The anodic peak currents were increased with the increasing nitrite concentration.

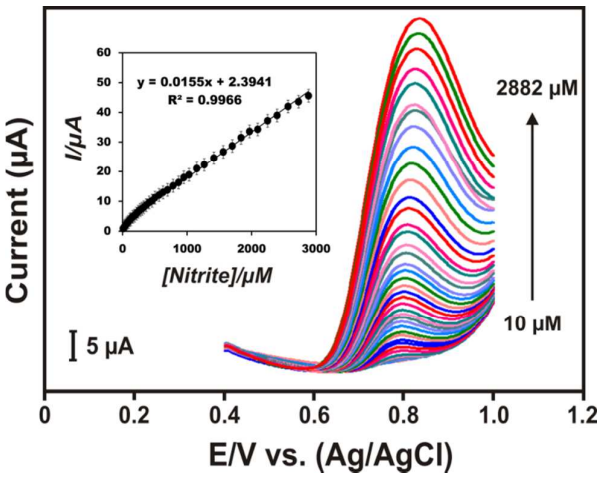

Fig. 11 DPV responses for 10 % of Fe_3O_4/RGO nanocomposite modified GCE at different concentrations of nitrite (10–2882 μM) in N_2 saturated 0.1 M PBS (pH 4). Inset is the corresponding calibration plot of response peak current vs. nitrite concentration

The inset Fig.10 (c) shows the linear dependence of I_{pa} vs. various concentration of nitrite which shows that the I_{pa} increases linearly with the concentration of nitrite. The linear regression equation can be expressed as I_{pa}= 0.0528x-0.1582 with correlation coefficient of R^2=0.9988, where x is the different nitrite concentration. Therefore, the results confirm that the 30% Fe_3O_4 loading on RGO nanocomposites modified GCE possess higher electrocatalytic activity for determination of nitrite efficiently.

3.2.2 Differential pulse voltammetry (DPV)

In order to obtain the higher sensitivity of the proposed nitrite sensor, the differential pulse voltammetry (DPV) method has been employed. Figure 11 shows the DPV response curves for the oxidation of nitrite at different initial concentrations with the optimal experimental conditions. The DPV response of 30 % Fe_3O_4 loaded on RGO nanocomposite modified GCE for the detection of nitrite with different concentrations of 10–2882 μM in the presence of 0.1 mM N_2-saturated PBS solution with pH 5. The oxidation of I_{pa} was observed at 0.8 V and the peak current was proportional to the concentration of nitrite. Moreover, the peak currents linearly increased with increasing nitrite concentration as shown in inset Fig.11. The linear regression equation is I_{pa} (μA) =0.015x + 2.39 with correlation coefficient of R^2 = 0.9966, where x is concentration of nitrite. The ca. sensitivity of nitrite is to be 196.2 μA mM cm^{-2}. The obtained sensitivity can be attributed to the low charge transfer resistance of the modified GCE and also the efficiency of the electron-transfer between nitrite due to the catalytic effect and modified GCE.

The detection limit can be calculated by the following equation (5)

$$LOD = \frac{3S_B}{b} \quad (5)$$

Where S_B is the standard deviation of the blank signal and b is the sensitivity. Based on the above experimental calculation the LOD is found to be 0.1 μM. Thus the results clearly confirm that the electrocatalytic analytical parameters of modified GCE are greater to those of other reported modified electrodes as show in Table 1.

3.2.3 Amperometric determination of nitrite

Furthermore, the amperometric (*i-t*) nitrite detection was also performed with optimized conditions with a rotating disc electrode (RDE) to obtain better sensitivity than DPV. Figure 12 (a) shows the typical amperometric responses of GCE modified with Fe_3O_4/RGO nanocomposite with successive addition of nitrite at an applied potential of 0.77 V. The *i-t* response was observed with modified GCE in a rotating speed of 300 rpm with successive additions of 0.5 μM to 9.56 mM nitrite in a continuously stirred 0.1 M PBS (pH 4) solution.

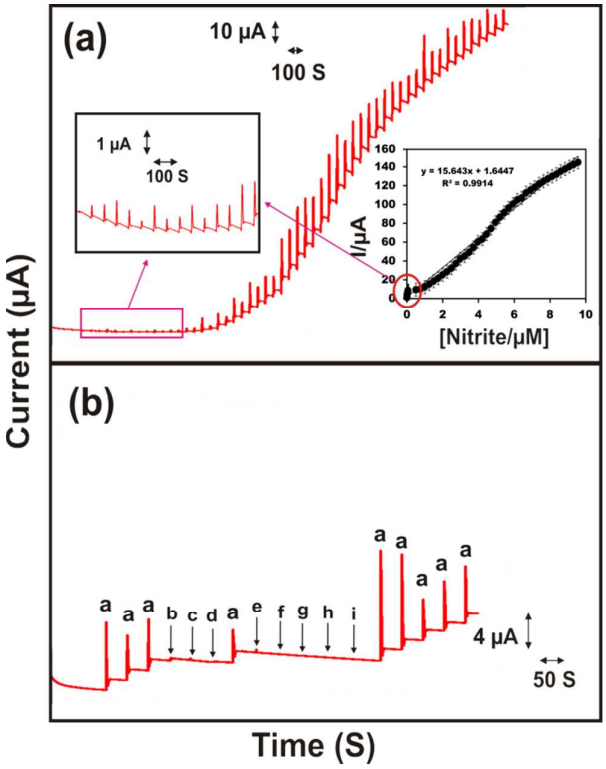

Fig. 12 (a) Amperometric response of nitrite at 30 % Fe_3O_4/RGO nanocomposite modified rotating-disc GCE with successive additions of 1mM nitrite into a continuously stirred 0.1 M PBS (pH 4) solution. Rotation speed: 1800 rpm; E_{app} = +0.77 V. The inset is the linear calibration plot of the dependence of the measured current (*i-t*) on various nitrite concentrations. (b) Steady-state current response obtained reduction for 25 μM of nitrite (a), urea (b), $NaNO_3$ (c), KCl (d), $ZnCl_2$ (e), $NiCl_2$ (f), glucose (g), $CoCl_2$ (h) and $FeCl_2$ (i) at 30 % of Fe_3O_4/RGO nanocomposite modified rotating-disc GCE.

Table 1. Analytical parameters of the Fe_3O_4/RGO-modified GCE toward nitrite sensor over various electrodes

Glassy carbon modified electrode	Limit of detection (μM)	Linear response range(μM)	Sensitivity ($\mu A \mu M^{-1} cm^{-2}$)	Techniques	Ref.
Fe_3O_4/RGO	0.1 0.03	10-2882 0.5-9563	196 ($\mu A m M^{-1} cm^{-2}$) 202.5 ($\mu A m M^{-1} cm^{-2}$)	DPV[b] Amperometry	**Present work**
RGO/MWCNTs/Pt/Mb	-	100 - 12000	0.16	Amperometry	27
GNPs/MWCNTs	0.01	0.05 – 250	2.58	DPV	28
Au NPs/SG	0.2	10 – 3960	0.045	Amperometry	29
Chemically reduced graphene oxide	1	8.9 – 167	0.026	Amperometry	30
Heteroatom-enriched activated carbon	0.07 0.13	0.1- 127 3 - 90	13.2 9	Amperometry DPV[b]	31

The amperometric current was increases linearly with increasing concentration of the nitrite. The inset in Fig 12 (a) shows the oxidation current was linear with the nitrite concentration in the range of 0.5 μM to 9.56 mM. The linear regression equation is I_{pa} (μA) =15.64*x* + 1.64 with correlation coefficient of R^2 = 0.9914, where x is concentration of nitrite. Interestingly, we obtained two different linear ranges of 0.5-58 μM, and a wide range of 0.5 μM–9.5 mM. The *ca.* sensitivity of nitrite is to be 202.5 μA L mM cm^{-2}. The limit of detection (LOD) was evaluated to be 0.03 μM by using eqn (5) and the analytical performances of the earlier reported nitrite sensors are also summarized in Table 1.

Table 2. Determination of nitrite in various water samples using DPV

Real samples	Analyte	Addition (μM)	Detection (μM)	Recovery (%)
Tap water	nitrite	25 100	24.8 97.5	96 ± 0.2 97.5 ± 1.2
Rain water	nitrite	25 100	25.5 101.5	102 ± 0.5 101.5 ± 1.5
River water	nitrite	25 100	26.2 105.2	104.8 ± 2 105.2 ± 1.8

These results clearly confirm the modified GCE detect the increasing concentration of nitrite that within 2 sec the response time reaches 97% of the steady state signal. This clearly indicates the modified GCE can efficiently be used as electrochemical sensor for the detection of nitrite. A well-defined and rapid amperometric responses was observed for each addition of 10 μM nitrite as shown in Fig.12 (b) for the modified GCE. But, there was no significant amperometric responses was observed for every 1000-fold additions of other compounds such as urea, $NaNO_3$, KCl, $ZnCl_2$, $NiCl_2$, glucose, $CaCl_2$ and $MgCl_2$, which reveals the good selectivity of the nitrite sensor at Fe_3O_4/RGO modified GCE.

The repeatability and reproducibility were experienced by measuring the amperometric response of 10 μM nitrite for ten measurements and the relative standard deviation was only less than 2.5%. The stability of the fabricated sensor was studied by using DPV by measuring the I_{pa} periodically and it retains 92.36% of its initial reduction of I_{pa} and after 25 days at room temperature shows good storage stability. Further, the interference for the determination of nitrite was examined by adding various organic and inorganic species in to the PBS solution with the pH of 4.

3.2.4 Real sample analysis

The fabricated sensor was further used to determine the nitrite from various water sources for real sample analysis. The samples were collected from different water sources such as tap, rain and river water followed by filtered with 0.50 μm membrane to remove the micron sized particles. The

nitrite concentration in tap, rain and river water is measured by using DPV by standard addition method. The results are tabulated in Table 2 and it shows the good recovery from 96 to 105.2%. It confirms the fabricated sensor is highly efficient for the industrial real time applications.

4. Conclusion

In conclusions, we have demonstrated a simple eco-friendly large scale production of layered graphene with less disordered structure in the presence of $KMnO_4$ and aspartic acid using high energy ball-mill. Further, the Fe_3O_4 nanoparticles with different weight percentage of 10, 20 and 30 % were loaded on graphene by hydrothermal process and studied their physico-chemical and functional properties. The magnetic behavior, size, shape and particle-particle interaction strongly depends on the concentration of the Fe_3O_4 nanoparticles on RGO. The physico-chemical properties confirm the possible growth may be due to the redox hybridization process. The obtained high specific surface area of 140 m^2g^{-1} and high insolubility of Fe_3O_4/RGO nanocomposite in aqueous solution favors the fabrication of sensing devices to use in water system. A highly sensitive and selective determination of nitrite was done by using differential pulsed voltammetry (DPV) and amperometry (*i-t*) based on Fe_3O_4/RGO-GCE. The modified GCE exhibits a lower detection limit and higher sensitivity of 0.03 µM and 202.5 µA $mM^{-1}cm^{-2}$, respectively. Besides, the practicability of the modified GCE has also been studied to determine the nitrite in tap, river and rain water and the results confirms the practical usage of the fabricated sensor.

Acknowledgements

The authors would like to acknowledge the University Grant Commission (UGC), Government of India, and New Delhi for the financial support and DST – PURSE, Government of India for FESEM facility.

References

1. D. C. Elias, R. V. Gorbachev, A. S. Mayorov, S. V. Morozov, A. A. Zhukov, P. Blake, L. A. Ponomarenko, I. V. Grigorieva, K. S. Novoselov, F. Guinea and A. K. Geim, *Nat Phys*., 2011, **7**, 701-704.
2. A.K. Geim, *Science*, 2009, **324**, 1530-1534.
3. H. Chen, M. B. Muller, K. J. Gilmore, G. G. Wallace, D. Li, *Adv. Mater*., 2008, **20**, 3557-3561.
4. Y. Zhang, T.-T. Tang, C. Girit, Z. Hao, M. C. Martin, A. Zettl, M. F. Crommie, Y. R. Shen, and F. Wang, *Nature*., 2009, **459**, 820.
5. K. S. Kim, A. L.Walter, L. Moreschini, T. Seyller, K. Horn, E. Rotenberg, and A. Bostwick., *Nature Mater*, 2013, **12**, 887.
6. K. S. Novoselov, V. I. Fal'ko, L. Colombo, P. R. Gellert, M. G. Schwab and K. Kim, *Nature*., 2012, **490**, 192–200.
7. C. Zongping, R. Wencai, G. Libo, L. Bilu, P. Songfeng and C. Hui-Ming, *Nature Mater*., 2011, **10**, 424-428.
8. T. Limmer, J. Feldmann, and E. Da Como, *Phys. Rev., Lett*, 2013, **110**, 217406.
9. K.Yang, L. Feng, H. Hong, W. Cai, Z. Liu, *Nat. Protoc*, 2013, **8**, 2392–2403.
10. V. Chabot, D. Higgins, A. Yu, X. Xiao, Z. Chen and J. Zhang, *Energy Environ. Sci*., 2014, **7**, 1564-1596.
11. H. Wang, T. Maiyalagan, and X. Wang, *ACS Catal*. 2012, **2**, 781-794.
12. O.Y. Posudievsky, O. A. Khazieieva, V. G. Koshechko and V. D. Pokhodenko, *J. Mater. Chem*., 2012, **22**, 12465-12467
13. V. Leo´n, A. M. Rodriguez, P. Prieto, M. Prato, and E. Va´zquez, *ACS Nano*, 2014, **8**, 563-571.
14. V. Chandra, J. Park, Y. Chun, J. W. Lee, I. C. Hwang and K. S. Kim, *ACS Nano*., 2010, **4**, 3979–3986.
15. Q. Qu, S. Yang and X. Feng, *Adv. Mater*. 2011, **23**, 5574-5580.
16. J. Shen, Y. Hu, M. Shi, N. Li, H. Ma, and Y. Mingxin, *J. Phys. Chem. C*., 2010, **114**, 1498-1503.
17. Y. Yunjin, Z. Yang, D. Zhang, W. Peng, H. Sun and S. Wang, *Ind. Eng. Chem. Res.* 2012, **51**, 6044-6051.
18. V. V. Singh , G. Gupta , A. Batra , A. K. Nigam , M. Boopathi , P. K. Gutch , B. K. Tripathi , A. Srivastava , M. Samuel , G. S. Agarwal , B. Singh , and R. Vijayaraghavan, *Adv. Funct. Mater*. 2012, **22**, 2352-2362.
19. G. Bharath, Rajesh Madhu, Shen-Ming Chen, Vediyappan Veeramani, M. Manivel Raja, A. Balamurugan, D. Mangalaraj, C. Viswanathan and N. Ponpandian, *RSC Adv*., 2015,**5**, 13392-13401.
20. Y. T. Kong, M. Boopathi and Y. B. Shim, *Biosens. and Bioelectron*, 2013, **19**, 227-232.
21. S. Ghosh, H. Remita, P. Kar, S. Choudhury, S. Sardar, P. Beaunier, P. Sarathi Roy, S. K. Bhattacharya and S. K. Pal., *J. Mater. Chem. A*, 2015, **3**, 9517–9527.
22. S. Ghosh, D. Ghosh, P. K. Bag, S. C. Bhattacharya and A. Saha., *Nanoscale*, 2011, **3**, 1139-1148.
23. G. Bharath, Rajesh Madhu, Shen-Ming Chen, Vediyappan Veeramani, A. Balamurugan, D. Mangalaraj, C. Viswanathan and N. Ponpandian, *J. Mater. Chem. B*, 2015,**3**, 1360-1370.
24. S. Ghosh, S. C. Bhattacharya and A. Saha, Anal. Bioanal. Chem., 2010, 397, 1573-1582.
25. S. Ghosh, M. Ray, M. R. Das, A. Chakrabarti, A. H. Khan, D. D. Sarma and S. Achary., Phys. Chem. Chem. Phys., 2014,16, 5276-5283
26. H. Teymourian, A. Salimi and S. Khezrian, *Biosens. and Bioelectron*, 2013, **49**, 1-8
27. V. Mani, B. Dinesh, S.M. Chen and R. Saraswathi, *Biosens. and Bioelectron*., 2014, **53**, 420-427.
28. Afkhami, F.S. Felehgari, T. Madrakian and H. Ghaedi, *Biosens. and Bioelectron*.,2014, **51**, 379-385.
29. S.J. Li, G.Y. Zhao, R.X. Zhang, Y. L. Hou, L. Liu and H. A. Pang, *Microchim Acta*., 2013, **180**, 821–827.
30. V. Mani, A.P. Periasamy and S.M. Chen, *Electrochem. Commun*., 2012, **17**, 75-78.
31. M. Rajesh, V. Veeramani and S. M. Chen, *Sci. Rep*., 2014, 4 , 4679.